A Preliminary Design Procedure for an Ion-Beam Shepherd Mission

Hodei Urrutxua[☆a,b], Claudio Bombardelli[b], José Manuel Hedo[b]

[a] *European Institute for Aviation Training and Accreditation, Rey Juan Carlos University, Fuenlabrada, Madrid, Spain*
[b] *Space Dynamics Group, Technical University of Madrid, Spain*

Abstract

The "ion-beam shepherd" (IBS) is a contactless active space debris removal technique, also applicable to asteroid deflection. In the design of an IBS mission many constraints need to be considered, which involve multiple trade-offs. These constraints can be expressed analytically as a function of certain design parameters, and conveniently displayed in a two-dimensional parameter space or design space. This construction yields a "matching chart", which effectively provides a feasible design envelope, and enables to find graphically a suitable design point that satisfies all applicable operational constraints simultaneously, thus providing a powerful tool tailored for the preliminary design of an IBS mission.

Keywords: Ion-beam shepherd, active space debris removal, preliminary design, design envelope

1. Introduction

Space Debris is a growing concern for the safe exploitation and utilization of space, as the population of spaceborn objects in the vicinity of the Earth keeps steadily increasing [1, 2]. In order to guarantee the sustainability of space as a resource for humanity, many efforts are being targeted at mitigating the space debris problem, which has resulted in an internationally agreed set of regulations

☆Corresponding author.
Email address: hodei.urrutxua@urjc.es (Hodei Urrutxua☆)

and guidelines [3, 4]. However, the large number of objects already in orbit and the predicted growth rate of the space debris population suggests that the latter measures will need to be complemented with Active Debris Removal (ADR) initiatives [5, 6, 7, 8, 9]. For the last decade ADR has been actively considered and a variety of novel ADR concepts have been devised, many of which are currently under development; Reference 10 provides a review and comparison of existing technologies on active space debris capturing and removal, along with an exhaustive list of relevant bibliographic resources.

Among ADR methods, the Ion Beam Shepherd (IBS) concept has emerged as a very promising technique for active space debris removal[11], as well as for asteroid deflection purposes [12, 13]. The concept relies on exploiting the momentum transmitted by a collimated beam of quasi-neutral plasma impinging against a target object, where the beam is generated by an ion thruster. Embarking a secondary thruster device onboard the IBS allows to maintain nearly constant the separation distance with respect to the target. The key advantages of this concept are[14]: i) it is a contactless method, so there is no need to dock or berth with a non-cooperative target, thus increasing the safety of operations; ii) the concept works independently of the target shape, material or rotation state; iii) it is reusable up to complete fuel depletion, thus enabling multi-target ADR missions; iv) the momentum transfer is very efficient due to the use of high specific impulse propulsion systems; and v) is based on mature and space-tested electric propulsion technology, with a high technology readiness level (TRL).

Although in principle conceptually simple, the IBS approach involves many interesting engineering challenges from the viewpoint of the dynamics and control. Additionally, many of the working principles of the concept, such as plasma-target interaction, the efficient momentum transfer and the controlled and reliable contactless deorbiting (or reorbiting) of a target object, need to be thoroughly tested and validated. Although some of these aspects could be effectively tested on ground, others cannot be properly reproduced and validated except in space, such as the dynamical and plasma environment in low-Earth orbit, or the correct functioning of the close range navigation and control algo-

rithms in a real scenario. For that purpose, an in-orbit demonstration mission will eventually be imperative for increasing the TRL of the IBS concept; i.e. a change in altitude of a spaceborn object has to be clearly demonstrated.

The conception of such a space mission entails, among other things, the preliminary design of an IBS spacecraft. The authors have addressed this task in recent years through various research projects[15], where the difficulties involved in the design of such a non-conventional and purpose-specific spacecraft became evident. Hence, the preliminary design methodology presented in this article was developed as an answer to this necessity and stems from the experience earned in so-doing. This methodology exploits the particular needs of an IBS mission and breaks from other approaches considered in the literature for the general problem of preliminary spacecraft design[16, 17, 18, 19], by offering a simpler and specifically tailored preliminary design solution for an IBS mission.

The design of an IBS mission involves various factors that need to be taken into account. These include considerations such as the onboard power availability, the thrust parameters of both the primary and secondary thrusters (thrust, divergence angle, specific impulse, ...), collision avoidance concerns, backsputtering contamination, mission lifetime, and a long etcetera. A trade-off involving all the aforementioned considerations should result in the selection of the design parameters, the most important of which are possibly the separation distance between the IBS and the target object, and the preliminary design of the main parameters of the propulsion and power subsystems.

The specific optimization of IBS subsystems has already been looked at, as by Cichocki et al. [20] who studied the optimization of the electric propulsion subsystem for an IBS mission. The latter study aimed at finding the optimal design points of both involved thrusters, whose design was not fixed a priori; in contrast, this article aims at the system-wide design of an IBS mission, assuming both thrusters are already selected (yet allowing to iterate for different choices of thrusters). However, Ref. [20] does not consider the interaction with non-propulsive mission constraints. In fact, the system-level optimization of an IBS mission has not yet been addressed in the literature. A fundamental first step

towards that goal is to have a reasonable initial guess to start the optimization process, i.e. an initial or preliminary design, for which approximate but quick techniques may be useful.

In the field of preliminary aircraft design, the thrust-to-weight ratio versus wing loading diagram is a paradigmatic example of the *matching chart* concept.[1] This diagram provides a convenient graphical representation of the operational limitations of the aircraft within the design space, shows the feasible design configurations and enables the selection of a suitable design point, and has become a standard tool for aircraft preliminary design[21]. Interestingly, this design envelope or matching chart concept can be conveniently extended to be applicable for the preliminary design of an IBS mission. For this end, graphical methods prove to be a powerful and intuitive tool to highlight the functional dependencies between various operational constraints, make a quick assessment of the current design, and if needed, provide guidelines to refine the design through successive iterations. At the preliminary design phase, the nominal operation point of the IBS mission must be wisely selected to comply with the various operational constraints and technological limitations that may apply, many of which are typically competing factors that require well-balanced trade-offs. These relationships between the many design parameters can be graphically displayed in an appropriate parameter domain that results in a low-dimensional design space, where system-level inter-dependencies can be easy interpreted and understood at a glance. Setting a nominal operation point in the design space is therefore equivalent to characterizing an IBS mission by fixing the main design parameters such that all relevant mission constraints are fulfilled; then, an iterative optimization process can follow to refine the preliminary design until a frozen configuration is reached, ultimately leading to the low-level design of the various subsystems.

The remainder of this article is organized as follows: In Section 2 the IBS

[1] The *flight envelope*, i.e. airspeed versus load factor diagram, is another archetypal example of a matching chart in aerospace engineering.

concept is briefly explained, the fundamental working principles are detailed and the basic equations are stated. In Section 3 the matching chart or design envelope of an IBS is introduced and a set of constraints is presented, which correspond to the limitations and boundaries imposed by individual subsystems or operational restraints. Section 4 presents an application example where the design envelope methodology is used for the preliminary design of an IBS mission. Finally, Section 5 covers further discussion on the use of the design envelope, and Section 6 summarizes the main conclusions.

A companion software application is provided along with this article, which implements the design procedure and algorithms presented herein in a MATHEMATICA interactive Computatable Document Format under the GNU GPL v3 license. This code is available at `http://sdg.aero.upm.es/ONLINEAPPS/IBS_Design`.

2. The Ion-Beam Shepherd Concept

An IBS satellite makes use of an onboard electric thruster to direct a plasma beam against a target object, typically a piece of space debris. As illustrated in Figure 1, the ion beam interacts with the target exerting a net surface force upon it, and thus transmitting a momentum to it. Consequently, the target object experiences an acceleration, which can be used to remotely displace the target, and potentially deorbit or reorbit it. In the general case, the target does not capture the totality of the plasma emanated from the thruster, since the plasma plume expands downstream and the target eventually receives only a fraction of the total momentum. Thus, the momentum transfer efficiency, η_B, is defined as the fraction of momentum captured by the target, or equivalently the ratio between the net force acting upon the target and the net force produced by the thruster. The thruster used to transmit momentum to the target is hereafter referred to as *primary* thruster or momentum transfer thruster. Thus, if F_1 is the force transmitted by the primary thruster, then $\eta_B F_1$ is the actual force exerted upon the target.

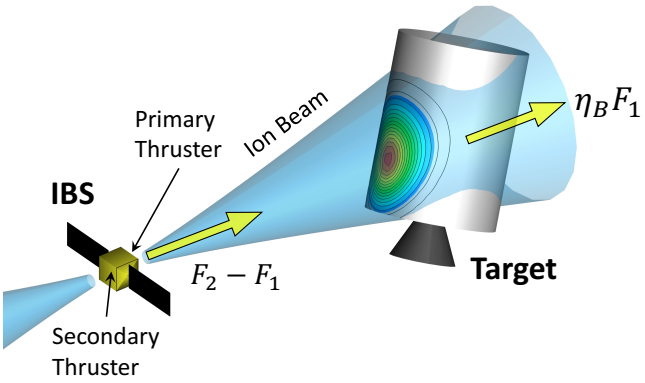

Figure 1: Illustration of an ion-beam shepherd deorbiting an upper stage.

The force F_1 also reacts upon the IBS satellite repelling it away from the target. Hence, if the IBS-target separation is to be maintained bound, a *secondary* thruster, a.k.a. thrust compensation thruster, will be needed to counteract this drift. This thruster exerts a force F_2 upon the IBS, which opposes that of the primary thruster, such that the net force upon the IBS is $F_2 - F_1$. It is assumed that both the IBS and the target nominally follow the same quasi-circular orbit, and thus under the Clohessy-Wiltshire approximation their relative motion is rectilinear and these net forces always act tangentially to the orbital velocity.

2.1. Relative Orbital Dynamics

In a deorbiting mission the IBS must be ahead of the target object, so the momentum received by the latter decelerates it and moves it into a lower altitude orbit following a quasi-circular trajectory. If all external perturbations are neglected, the relative acceleration upon the target, a_T, is solely due to the ion-beam interaction, and satisfies

$$a_T = \eta_B \frac{F_1}{m_T}$$

where m_T is the mass of the target object. Equivalently, the relative acceleration upon the IBS produced by the difference in thrust between the primary and secondary thrusters is

$$a_S = \frac{F_2 - F_1}{m_S}$$

where m_S is the mass of the IBS spacecraft.

Nominally the IBS needs to follow the target object maintaining a constant separation distance, therefore both accelerations must coincide, $a_T = a_S$. This yields a relation between the momentum transfer efficiency, η_B, and the thrust values of both thrusters. Isolating F_2, this relation may be written as

$$F_2 = F_1 \left(1 + \eta_B \frac{m_S}{m_T}\right) \tag{1}$$

and it becomes evident that $F_2 \geqslant F_1$ during the deorbiting operation. Also, both thrusters are assumed to provide a constant thrust, whereas the momentum transfer efficiency depends mainly on the debris center of mass location relative to the shepherd.

2.2. Plasma Plume and Momentum Transfer

The far-field expansion of the plasma plume of a thruster has been extensively studied (see Ref. 22 and references therein). An element of vital importance is the interaction of the ion beam with the target object and the quantification of the momentum transferred to the target. This interaction is extremely complex to model accurately [23, §3], but approximate expressions will do for the purpose of preliminary design. Under the simplifying assumptions of a conical plasma plume (i.e. neglecting electron pressure effects) and a spherical target body placed along the centerline of the plasma plume, Bombardelli et al. [24, 14] proposed the following exact analytical solution (*cannonball* model) for the momentum transfer efficiency:

$$\eta_B\left(\rho\right) \simeq 1 - \exp\left(\frac{-3\,R_T^2}{(\rho^2 - R_T^2)\,\tan^2\varphi}\right) \tag{2}$$

where ρ is the nominal separation distance of the target relative to the shepherd, φ is the divergence of the plasma plume, and R_T is the radius of the spherical target body (or the radius of an equivalent sphere in the case of non-spherical objects). Note that this equation assumes isothermal electrons, which is a conservative assumption, since it yields a higher divergenge increase than for a more realistic polytropic electron fluid.

The angle φ is not constant as the plume tends to deviate from a cone owing to thermal effects that translate into electron pressure effects; this can be taken into account by the relation

$$\tan\varphi \approx \sqrt{\tan^2\varphi_0 + \epsilon^2 \ln\left(\epsilon\,\frac{\rho}{R}\right)}$$

where φ_0 is the initial divergence at the exit of the thruster and

$$\epsilon = \frac{12\,q_e\,T_e}{I_{\mathrm{sp}}^2\,g^2\,m_i}$$

quantifies the influence of the temperature T_e (eV) of the beam neutralizing electrons, measured at a reference beam cross-section of radius R, on the far-field beam divergence. In the above equation I_{sp} is the thruster specific impulse (measured in seconds), q_e is the electron charge, $g = 9.81\ \mathrm{m\,s^{-2}}$ is the sea level gravity and m_i the ion mass of the propellant.

Alpatov et al. [25] proposed a more sophisticated model capable of estimating the force transmitted to a body of arbitrary shape, which needs to be evaluated numerically and depends on the attitude of the target object. Also, Cichocki et al. [26] have recently proposed a fully numerical model, where both the plume simulation and the interaction with the target debris is numerical and attitude/shape dependent. In practice, however, Eq.(2) proves both convenient and sufficient for the purpose of preliminary design.

2.3. Power and Propulsion System

The overal performance of an electric space propulsion device (typically an ion thruster or Hall effect thruster) can be characterized from its thrust, F, and flow rate, $\dot{m}$. Throtability is a common feature of modern thrusters, so these propulsive magnitudes can vary with the regime of operation, which is ultimately controlled by the electrical power supplied to the thruster, P. The selection of the thrust and flow rate as control parameters proves convenient since theoretically both vary linearly with the electrical input power (assuming grid voltage and other parameters remain constant), as illustrated in Figs. 2a

and 2b. Indeed, experience shows that thrust can be reliably modeled with a linear law of the power, whereas there is a benefit in adjusting the mass flow with a quadratic fit instead, as this yields a better correlation with experimental data, despite the quadratic term being typically very small. Hence, in the following we shall assume that the thrust and flow rate of each thruster can be modeled as

$$F(P) = \alpha + \beta\, P \tag{3}$$

$$\dot{m}(P) = \alpha' + \beta'\, P + \gamma'\, P^2 \tag{4}$$

where the polynomial coefficients are fit parameters that can be estimated from mathematical models or measured experimentally. In particular, α and β can be inferred from the lower and upper working limits of the thruster; i.e. if the thrust $F \in [F_{\min}, F_{\max}]$ and the power $P \in [P_{\min}, P_{\max}]$ supplied to each individual thruster are known, then

$$\alpha = F_{\min}\left(1 - \frac{F_{\max}/F_{\min} - 1}{P_{\max}/P_{\min} - 1}\right), \qquad \beta = \frac{F_{\max} - F_{\min}}{P_{\max} - P_{\min}}$$

If the flow rate is assumed linear, then $\gamma' = 0$ and coefficients α' and β' can be obtained analogously. In most cases, such simplification yields fairly small errors (see Fig. 2b) and might therefore be a reasonable hypothesis for preliminary design purposes while also simplifying the forthcoming mathematical derivations.

Another meaningful parameter related to the propulsive performance of a thruster is the specific impulse, I_{sp}, which is related to both the thrust and the flow rate by means of

$$F = \dot{m}\, I_{\text{sp}}\, g \tag{5}$$

From Eqs. (3-4), the specific impulse can be expressed as a function of the power supply as

$$I_{\text{sp}}(P) = \frac{\alpha + \beta\, P}{g\,(\alpha' + \beta'\, P + \gamma'\, P^2)}. \tag{6}$$

Note that I_{sp} is a non-linear function of the input power (see Fig. 2c). Interestingly, since Eq. (3) is linear, it can be easily inverted to provide the input

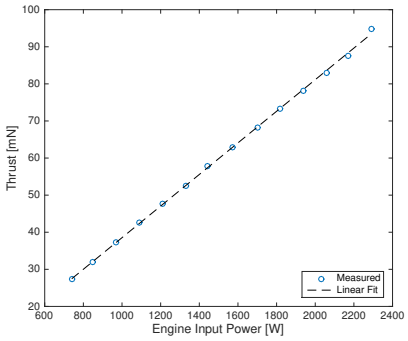

(a) Thrust: $F(P)$.

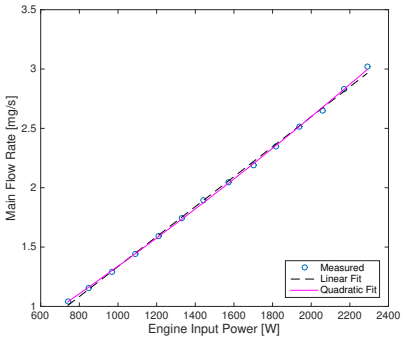

(b) Flow rate: $\dot{m}(P)$.

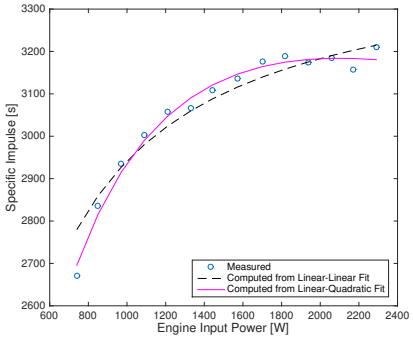

(c) Specific impulse: $I_{\mathrm{sp}}(P)$.

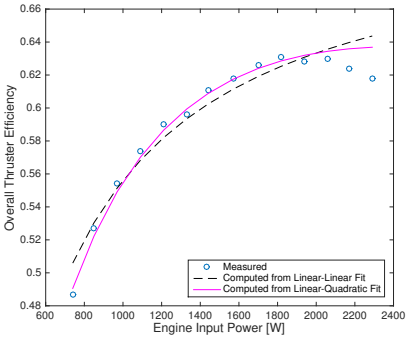

(d) Thruster efficiency: $\eta_T(P)$.

Figure 2: Performance curves for NSTAR thruster at standard temperature and pressure [27]. Both linear and quadratic fits are displayed for F and $\dot{m}$. For I_{sp} and η_T, the approximations are not fitted to measurements but instead computed from Eqs. (6) and (8) respectively, and two approximations are shown: one relying on linear fits of the thrust and mass flow, referred to as 'Linear-Linear Fit' (dashed line), and another where a quadratic fit is assumed for the mass flow ($\gamma' \neq 0$), referred to as 'Linear-Quadratic Fit' (solid line).

power as a function of thrust, i.e. $P = (F - \alpha)/\beta$, which allows to alternatively express the specific impulse as a function of thrust:

$$I_{\mathrm{sp}}(F) = \frac{\beta^2 F}{g\left[\beta^2\alpha' + \beta\,\beta'\,(F-\alpha) + \gamma'\,(F-\alpha)^2\right]}. \tag{7}$$

Yet another relevant propulsive magnitude is the overal thruster efficiency, η_T, which measures the fraction of the electrical energy supplied to the thruster that gets effectively converted into useful kinetic energy imparted to the spacecraft[14],

i.e.

$$\eta_T \, P = \frac{1}{2} \, g \, I_{\mathrm{sp}} \, F.$$

Using Eqs. (3-6) the thruster efficiency can be expressed as a function of the input power:

$$\eta_T(P) = \frac{(\alpha + \beta \, P)^2}{2P \, (\alpha' + \beta' \, P + \gamma' \, P^2)}. \tag{8}$$

Equally, the thruster efficiency can also be expressed as a function of thrust by inverting Eq. (3). Note that η_T is also non-linear, yet Eq. (8) yields a fair approximation throughout the operation domain of the thruster (see Fig. 2d).

Note that the quadratic fit for the mass flow rate ($\gamma' \neq 0$) provides only a marginal improvement in Fig. 2b, but this quadratic term enables to capture higher order non-linearities in derived quantities such as the specific impulse (Fig. 2c) or the overall thrust efficiency (Fig. 2d), as compared to the linear fit ($\gamma' = 0$).

An IBS spacecraft will require that primary and secondary thrusters provide a different thrust magnitude, as deduced from Eq. (1). In the following, the study can be conveniently (yet realistically) simplified by assuming that both thrusters of the IBS are physically equal (i.e. parameters α, β, α', β' and γ' are the same for both thrusters), but operate at different power levels. Thus, hereafter we shall assume the primary thruster operates at a power level P_1 and the secondary thruster operates at a power level P_2, so each thruster will provide a different thrust, specific impulse and thruster efficiency. Consequently, Eq. (1) has its counterpart in terms of electrical power, which dictates at what power level the secondary thruster must operate in order to maintain a constant relative distance between the shepherd and the target:

$$P_2 = P_1 + \left(\frac{\alpha}{\beta} + P_1 \right) \eta_B \frac{m_S}{m_T}. \tag{9}$$

It is worth noting that assuming physically equal thrusters is, from a system level perspective, a reasonable assumption for the purpose of a preliminary design. However, using equal thrusters for both impulse transmission and compensation is suboptimal from the viewpoint of the Power and Propulsion System,

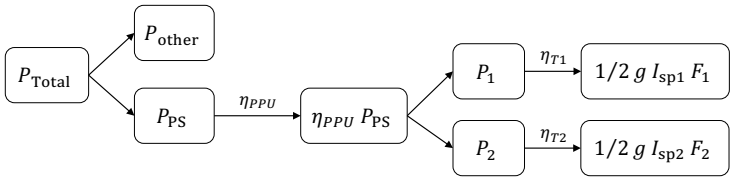

Figure 3: Schematic break-down of the power budget of an IBS spacecraft.

since as shown in Ref. [20] the optimal solution would require a very high I_{sp} impulse transfer thruster, and a relatively low I_{sp} secondary thruster, in order to reduce the overal power requirement (and thus the spacecraft mass) for a given separation distance and mission time.

A particular feature of an IBS spacecraft is that it simultaneously operates two main thrusters, which imposes a high demand of power supply onboard the spacecraft. Hence, the propulsive system will require an overal energy supply, P_{PS}, which encompasses the energy necessary to operate both, the primary and secondary thrusters, i.e.

$$\eta_{\text{PPU}}\, P_{\text{PS}} = P_1 + P_2$$

where η_{PPU} represents the power and propulsion unit conversion efficiency and is typically constant (a value of ~ 0.9 can be inferred from Ref. [27]). The former equation can be combined with Eq. (9) to provide the actual electrical power supplied to the propulsion system as a function of the power supplied to the primary thruster:

$$P_{\text{PS}}(P_1) = \frac{2P_1}{\eta_{\text{PPU}}} + \left(\frac{\alpha}{\beta} + P_1\right) \frac{\eta_B}{\eta_{\text{PPU}}} \frac{m_S}{m_T}. \tag{10}$$

Alternatively, the power supplied to the propulsion system can be expressed as a function of the thrust of the primary thruster:

$$P_{\text{PS}}(F_1) = \frac{F_1}{\beta\, \eta_{\text{PPU}}} \left(2 + \eta_B \frac{m_S}{m_T}\right) - \frac{2\alpha}{\beta\, \eta_{\text{PPU}}}. \tag{11}$$

Finally, it has to be taken into account that an IBS spacecraft will need to supply electrical power to many other onboard systems besides the propulsion system. Thus, the power budget will need to accomodate a higher energy demand to keep the spacecraft running. For short, the total power supply onboard

an IBS needs to be

$$P_{\text{Total}} = P_{\text{PS}} + P_{\text{other}}$$

where P_{other} represents the combined actual energy demand of all other subsystems onboard the shepherd satellite. This power budget can be used to size the solar arrays and estimate the size of the shepherd spacecraft. Figure 3 displays a schematic break-down of the onboard power budget throughout different levels of the subsystems of an IBS spacecraft.

2.4. Spacecraft Mass

The total mass of the shepherd spacecraft, m_S, is a key parameter for the preliminary design of an IBS mission, since it impacts the spacecraft dynamics and the relative orbital motion, which consequently imposes requirements upon the propulsion system, and ultimately affects the power budget, which links to the shepherd spacecraft sizing and its mass. Hence, it is a parameter whose influence spans throughout the design at all levels, and is one of the main outputs of the preliminary design process.

The power and propulsion system, including the propulsion plant and propellant tanks, solar arrays, batteries and auxiliary energy conversion and management systems, will need to be sized according to the total power budget computed in the preceeding subsection, also accounting for the degradation of these elements over the mission lifetime. The same is true for other subsystems (e.g. thermal, attitude & orbit control, structure, ...), which also need to be sized proportionally to the spacecraft mass, and are thus influenced by the power demand. Therefore, the mass of the spacecraft bus ultimately correlates with onboard power requirements, and experience shows that this correlation is roughly linear with the total power budget. Thus, a simple, yet effective sizing law provides the following estimate for the shepherd spacecraft mass[14]

$$m_S \simeq \alpha_P \cdot P_{\text{Total,max}} + m_0 + m_{\text{prop}} + m_{\text{prop,RCS}} \tag{12}$$

where α_P is the inverse specific power (in $\mathrm{kg\,kW^{-1}}$) and $P_{\mathrm{Total,max}}$ is the maximum total power for which the shepherd needs to be sized. m_0 is the constant term of the linear approximation to the dry mass of the spacecraft, which to a big extent (but not solely) accounts for the structure mass, so it might be conceptually useful to think of it as essentially the platform mass; it is in any case a known quantity for the designer. m_{prop} is the mass of propellant for the main thrusters, which needs to be estimated based on the mission duration, and $m_{\mathrm{prop,RCS}}$ is the propellant mass spent by the reaction and control system to maintain the coorbiting formation throughout the mission, and can be roughly estimated as a fraction of the former. More refined sizing guidelines exist for individual spacecraft subsystems, as shown in Ref. 16, but the simple law of Eq. (12) suffices for the purpose of this study.

The propellant mass for each thruster can be estimated from integrating Eq. (5), which yields

$$m_{\mathrm{prop}} = \frac{F\,(1-\chi)\,\Delta t}{I_{\mathrm{sp}}\,g}$$

where Δt is the mission lifetime and χ is the eclipse fraction, i.e. the fraction of the orbital period where the spacecraft is in eclipse; this assumes that main thrusters do not operate during eclipses since the power availability is limited. When both thrusters are considered, each operating at a different power level, the total propellant mass yields

$$m_{\mathrm{prop}} = \frac{F_1\,(1-\chi)\,\Delta t}{g\,I_{\mathrm{sp,1}}}\left[1+\frac{I_{\mathrm{sp,1}}}{I_{\mathrm{sp,2}}}\left(1+\eta_B\frac{m_S}{m_T}\right)\right]. \tag{13}$$

Thus, by virtue of Eq. (13) and the relations (1-2), the propellant mass is ultimately a function of F_1 and ρ, and therefore, so is the spacecraft mass, m_S. However, electric thrusters have a high specific impulse, and thus in practice the propellant mass only accounts for a small fraction of the total mass of the shepherd; consequently, disregarding the aforementioned dependence proves advantageous, and one can find an estimate for m_{prop} which remains fixed regardless of the values of F_1 and ρ. A fair simplifying assumption is to consider that the specific impulse is roughly equal for both thrusters. Therefore, in order to obtain a conservative estimate, we shall assume that both thrusters operate

at their maximum power level, where the mass flow is maximum, and it can also be assumed that $\eta_B \simeq 1$. Yet a final remark is that in Eq. (13) the propellant mass is expressed as a function of the total shepherd mass, m_S, which depends on m_{prop} through Eq. (12), and thus Eq. (13) is implicit in m_{prop}. Although an explicit relation can be found for m_{prop} combining Eqs. (12-13), for the sake of simplicity, one can just disregard the contribution of the propellant mass in the right-hand side, which yields the following estimate:

$$m_{\text{prop}} \simeq \frac{F_{\max}\,(1-\chi)\,\Delta t}{g\,I_{\text{sp}}(P_{\max})}\left(2+\frac{\alpha_P \cdot P_{\text{Total,max}}+m_0}{m_T}\right). \tag{14}$$

Since this is already a conservative estimate, it might not be necessary to account for additional margins.

2.5. Backsputtering Contamination

The IBS points a stream of plasma directly towards the target object. The interaction between the incident particles emanating from the thruster and the solid surface of the target object can give rise to many different phenomena, which will be determined by the kinetic energy of the incoming particles; typically, the *sputtering* phenomenon will be the predominant outcome of this interaction.

Physical sputtering is an atomic scale process that can occur if the incident particle (ion) can transfer sufficient energy to a surface or bulk target atom to overcome its bulk displacement energy and/or its surface binding energy. The erosion due to physical sputtering is described by the sputtering yield, a statistical variable defined as the mean number of atoms removed from a solid target per incident ion[30]. The modeling of sputtering yield is very complex and depends on the incidence angle, energy of incident ions, and properties of both ion and target materials. Furthermore, the flow of material backsputtered from a surface has a strong directionality, described by the differential sputtering yield[31]. Thus, the calculation of the backsputtering flow between complex geometries typically needs to be modeled numerically.

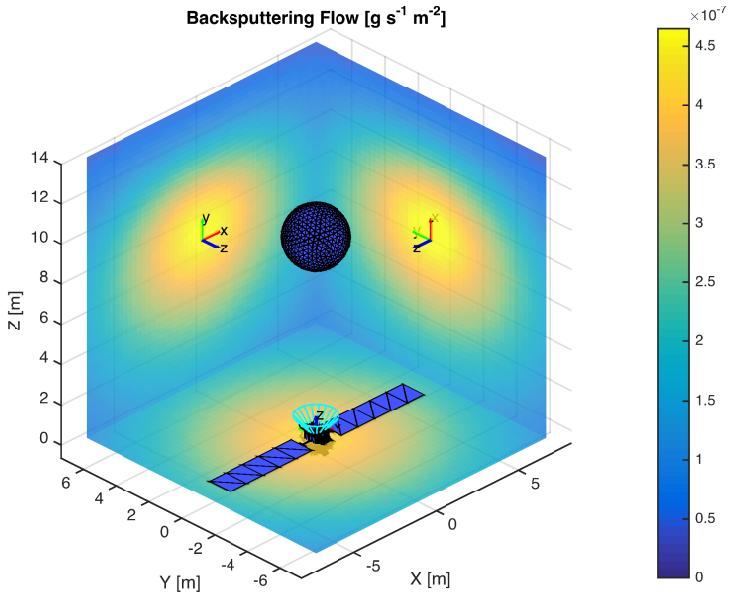

Figure 4: Simulation of backsputtered recoil flux performed with the in-house developed IBIS software [28, 29]. The strong dependence of the sputtering yield with the ion incidence angle, combined with the strong directionality of the spatial sputering recoil flux, results in the displayed backsputtering distribution, with maxima placed at the spacecraft and closely matching the perpendicular directions to the ion beam axis. The simulation considers an aluminum sphere of 1.5 m radius and a 30 mN thruster with an I_{sp} of 3400 s.

As illustrated in Figure 4, the backsputtering flow upon the IBS can potentially contaminate sensitive surfaces, like solar arrays or optical sensors, and thus limit the lifetime of the mission[28]. The backsputtering contamination can be assessed by estimating the cumulative backsputtered material flux that crosses through a prescribed reference surface located on the IBS spacecraft.

Under the assumption of a conical plasma plume and a spherical target body of radius R_T located at a distance ρ along the centerline of the plasma plume (see Figure 4), the backsputtering flux through the center of the IBS can be approximated by

$$\Phi\left(F_1,\rho\right) \simeq \phi \tanh^{\sigma}\left(F_1\right) \frac{R_T^2\left[\left(6\rho^2 - R_T^2\right)\tan^2\varphi - 3R_T^2\right]}{\rho^6\,\tan^3\varphi} \tag{15}$$

This approximation is valid for $R_T/\rho \ll 1$, where ϕ and σ are fitting parameters

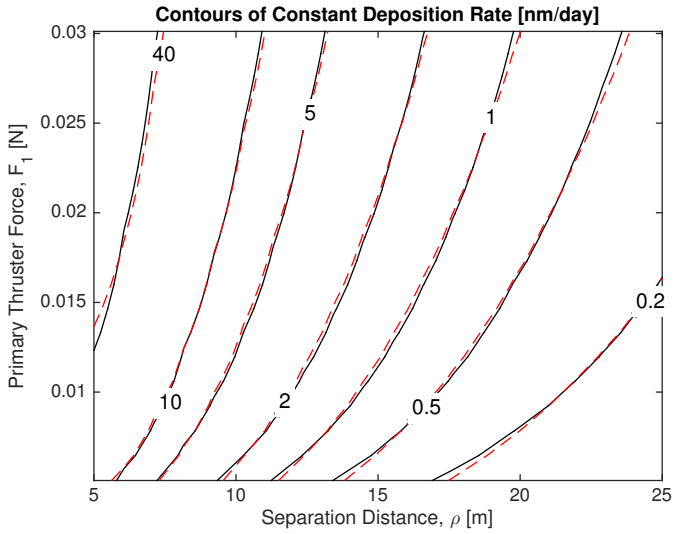

Figure 5: Contour lines of constant deposition rate of backsputtered material for a 1.5 m radius spherical aluminum target. Black solid lines are values simulated with IBIS [28, 29]. Red dashed lines are obtained from the analytical approximation.

that depend on the thruster characteristics, the plasma characteristics and the target object shape and material. A full derivation of Eq. (15) is presented in Appendix A . For a typical xenon thruster with $\varphi = 15°$, $F = 5\,\mathrm{mN}$ to $30\,\mathrm{mN}$, $I_{\mathrm{sp}} = 2550\,\mathrm{s}$ to $3400\,\mathrm{s}$, and an aluminium target surface, these parameters roughly take the values: $\phi \approx 1/145\,\mathrm{kg\,m^{-2}\,s^{-1}}$ and $\sigma \approx 6/5$. Figure 5 illustrates that the analytical approximation of Eq. (15) performs notably well even at relatively close distances to the IBS spacecraft.

Dividing Eq.(15) by the density of the target object material, ϱ_T, the backsputtering flux can be translated into an equivalent deposition rate of the backsputtered material. Thus, the growth rate of the thickness h of the backsputtered contaminant layer deposited on a virtual reference surface located at the center of the IBS is given by

$$\dot{h}\left(F_1, \rho\right) = \frac{\Phi\left(F_1, \rho\right)}{\varrho_T} \tag{16}$$

As a consistency check for the validity of the presented analytical model,

Ref. [26] predicts a contamination layer of 3 μm in 170 days for a cubic aluminum target object placed at 7 m and a thrust of 30 mN, whereas Fig. 5 provides 6-7 μm (40 nm/day during 170 days). This difference is not only attributable to the different models considered, but also to the different shape of the target object (the incidence on a cube is always normal and thus the average particle yield is lower), and therefore consistent, despite the simplifying assumptions of our analytical approximation.

Note the interaction of the backsputtering flow with the plasma plume is omitted. Also, placing the virtual reference surface at the center of the IBS yields an upper bound to the backsputtering contamination, which provides highly conservative estimates of the contamination upon other areas of the IBS spacecraft. Consequently, evaluating the backsputtering contamination off the IBS-target centerline would substantially decrease (up to orders of magnitude) the value of the fitting parameter ϕ. Therefore, the location of sensitive surfaces of the shepherd spacecraft must be selected based on the incoming backsputtering flow, i.e. they need to be placed where ϕ is sufficiently small to withstand the mission duration. Another immediate implication of Eq. (15) is that the best way to mitigate the contamination issue is to increase the target-shepherd separation distance while trying to reduce the beam divergence, in order not to compromise the momentum transfer efficiency.

2.6. Mission Lifetime and Orbital Decay Rate

The lifetime of an IBS mission also imposes constraints to the design. If an IBS mission is designed to deorbit (or reorbit) a given object, then the mission lifetime, Δt, is essentially equal to the actual deorbiting (or reorbiting) time, plus the time the shepherd is in eclipse and cannot operate the thrusters due to a limited power availability. Under the assumption of quasi-circular orbit and a constant deorbiting force directed along the tangent to the orbit, the deorbiting time is[11]

$$\Delta t\left(F_1,\rho\right)=\frac{m_T\sqrt{\mu}}{\eta_B(\rho)\,F_1(1-\chi)}\frac{\sqrt{r_0}-\sqrt{r_f}}{\sqrt{r_0\,r_f}} \tag{17}$$

where μ is the gravitational parameter of the Earth, χ is the eclipse fraction, r_0 is the initial orbital radius and r_f is the final orbital radius of the deorbiting phase. Note that swapping r_0 and r_f in Eq. (17) yields the reorbiting time. The eclipse fraction can be computed as

$$\chi = \frac{1}{\pi} \arcsin\left(\frac{R_{\text{Earth}}}{r}\right)$$

where R_{Earth} is the Earth radius and r is the instantaneous orbital radius; a conservative value for χ can be estimated by taking $r = \min(r_0, r_f)$. Note, however, that the eclipse fraction depends on the orientation of the orbital plane; in particular, the former eclipse formulation corresponds to the worst case scenario on which the orbital plane contains the anti-sun direction, while certain Sun-synchronous orbits have no eclipses.

Another concept linked to the mission lifetime is that of the decay rate (or conversely, the ascent rate), $\dot{r}$, which under the aforementioned hypotheses can be aproximated as[14]

$$|\dot{r}| \simeq 2\frac{\eta_B F_1}{m_T}\sqrt{\frac{r^3}{\mu}}. \tag{18}$$

Typically, an IBS mission would aim to deorbit more than a single object throughout the mission. Hence, in a multi-target IBS mission the shepherd would first rendezvous with an object, deorbit it, then reorbit itself to rendezvous with the next target object to be deorbited, and so on.

3. Design Envelope of an IBS

The design envelope or operational envelope of an ion-beam shepherd mission will be delimited by the domain of definition of its key design parameters, where these take feasible values and satisfy all applicable constraints regarding the IBS-target relative orbital motion, control, power and propulsion system characterization and other criteria. In order to identify these functional constraints, it is of the uttermost importance to: 1) identify the main variables involved in the description of the dynamics or the characterization of the relevant subsystems; 2) select the most appropriate or meaningful of these variables

as the design parameters; and 3) set the boundaries or operational limits where the IBS operations are feasible and safe. These constraints, mapped in the domain of the design parameters (i.e. the design parameter space), will provide the design envelope or matching chart, i.e. the range of the design parameters where the mission concept is viable or realizable.

From the set of variables explicitly involved in the dynamical description of the IBS-target relative dynamics and the characterization of the power and propulsion system, it will suffice to pick up two of them as the main design parameters, thus creating a suitable two-dimensional design space. The choice of the design parameters should be based on their relevance for design purposes, i.e. varying these variables along their range of definition should transcend into meaningful variations of the IBS mission concept that are insightful for the designer. After exploring combinations of the aforementioned variables, we came to the conclusion that the preferred design parameters are: the nominal IBS-target operational distance along the ion-beam, ρ, and the thrust of the primary thruster, F_1. Note that, alternatively, F_1 could be easily replaced by P_1 as a design parameter by means of Eq. (3), which only entails a linear transformation.

In the following, a comprehensive set of operational constraints $\mathcal{C}^{(i)}(F_1, \rho)$ is presented, which may apply to a typical IBS mission. These are defined such that positive values of the constraint equations represent feasible solutions, whereas negative values represent a violation of the constraint. Though some of the constraints rely on simplistic physical assumptions, the underlying concepts may be easily extended to accommodate models of higher complexity.

3.1. Collision Avoidance

Collision avoidance considerations may impose safety limitations to proximity operations in the vicinity of the target. Hence, the simplest form of a collision avoidance constraint can be seen as a proximity threshold limitation,

preventing the IBS to operate at distances below ρ_{col}, namely

$$\mathcal{C}^{(1)}(F_1, \rho) \equiv \rho - \rho_{\text{col}} \geqslant 0. \tag{19}$$

It is typically assumed that $\rho_{\text{col}} > (R_T + R_S)/2$ as a bare minimum, where R_S is the reference radius of the IBS spacecraft, although this distance might be set to a larger value, e.g. to consider spacecraft appendages or to set a conservative threshold. Thus, feasible IBS mission designs will need to operate at distances $\rho \geqslant \rho_{\text{col}}$ from the target to satisfy this safety requirement. This constraint visualizes in the design space as a vertical line delimiting feasible and unfeasible solutions (see Figure 6).

Additional collision avoidance considerations may suggest that the IBS is agile enough to react under the risk of any sudden and unexpected proximity to the target object, e.g. due to an actuator fault. The design of the IBS allows to accomplish this by switching off one the two main thrusters in order to gain an effective net force that moves the IBS into a safety distance.

3.2. Sensor Sensitivity

In practice, it is vital to equip an IBS spacecraft with a complete set of sensors to track the target body position and attitude with respect to the shepherd and the ion beam, and to be able to provide reliable metrology information to enable the autonomous target characterization, as well as the pose and position estimation capabilities to ensure safe operations, formation keeping and circumnavigation about the target. Thus, the sensing capabilities of the on-board Guidance, Navigation and Control (GNC) system may also impose limitations to the operational distance with respect to the target. Most commonly, when the IBS and target are too far apart, sensors may not be able to provide sufficiently accurate readings if the nominal design of the GNC algorithms is conceived for a closer operation range. In this regard, the sensitivity of the sensors may translate in a threshold value ρ_{sen} that limits the maximum allowable separation distance during nominal operation (see Figure 6). Thus, this constraint takes

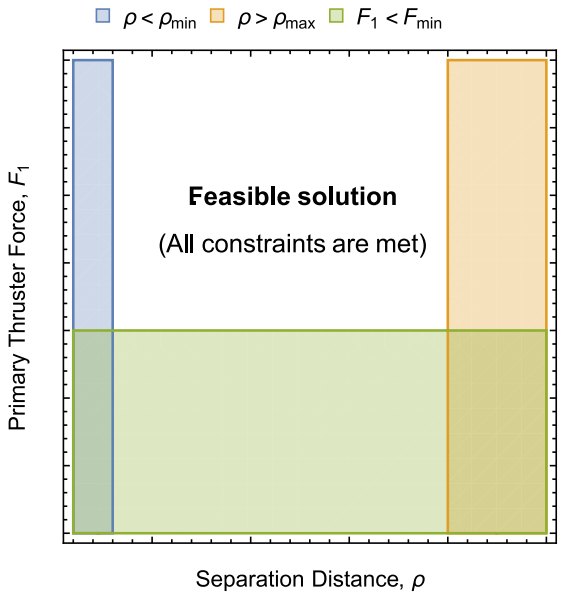

Figure 6: Feasible solution domain as delimited by different constraints. Colored areas correspond to regions violating the indicated constraints.

the form:

$$\mathcal{C}^{(2)}(F_1, \rho) \equiv \rho_{\text{sen}} - \rho \geqslant 0. \tag{20}$$

3.3. Minimum Momentum Transfer Efficiency

It may be reasonable to impose a minimum value to the momentum transfer efficiency, $\eta_{B,\min}$, to exclude from the search space solutions that would yield a poor or inadmissible momentum transfer efficiency. The condition $\eta_B(\rho) \geqslant \eta_{B,\min}$ is equivalent to the constraint:

$$\mathcal{C}^{(3)}(F_1, \rho) \equiv \rho_{\eta_B} - \rho \geqslant 0 \tag{21}$$

where ρ_{η_B} is the maximum separation distance that ensures the minimum desired efficiency. Hence, this constraint is formally analogue to that imposed by the sensor sensitivity.

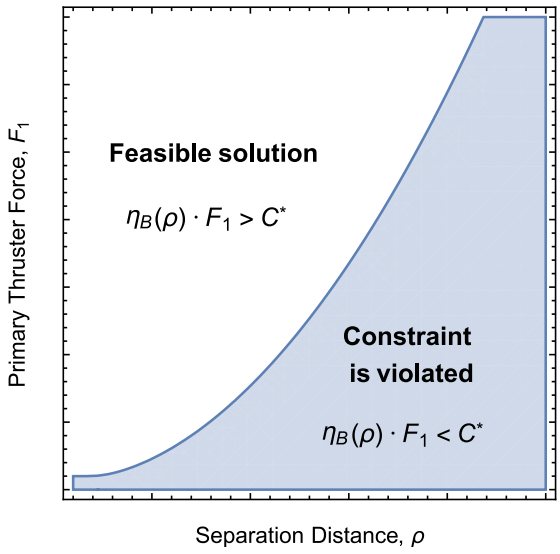

Figure 7: Region of the design space delimited by a constraint of the type $\eta_B(\rho) \cdot F_1 \geqslant C^*$.

3.4. Minimum Thrust

As discussed earlier, typical thrusters may vary their thrust level between the minimum and maximum operational values, $F_{\min}$ and $F_{\max}$ respectively; this is controlled by the supplied power level according to Eq. (3). Consequently, thrusters cannot operate at a power $P < P_{\min}$, thus setting the following constraint to the primary thruster:

$$\mathcal{C}^{(4)}(F_1, \rho) \equiv F_1 - F_{\min} \geqslant 0. \tag{22}$$

This constraint draws a horizontal boundary in the design space, such that feasible solutions may only exist above this limiting value of the primary thrust (see Figure 6).

3.5. Signal-to-Noise Ratio with Respect to Atmospheric Drag

In order to monitor the progress and efficiency of the deorbiting process, it is necessary to reliably measure the actual momentum transferred to the target.

In low Earth orbit, if the IBS is operating at large distance or low momentum transfer efficiency, the effects of the atmospheric drag could outweigh the momentum exchanged with the ion beam, and hence the actual deorbiting accomplished by the IBS could become indistinguishable from the atmospheric effects. Thus, it seems reasonable to impose the constraint that the ratio between the acceleration transmitted to the target and the acceleration exhibited due to the atmospheric drag must stay above a prescribed signal-to-noise ratio, SNR, namely:

$$\mathcal{C}^{(5)}(F_1, \rho) \equiv \frac{\eta_B(\rho)\, F_1}{F_{\text{drag}}} - \text{SNR} \geqslant 0 \tag{23}$$

where the momentum transfer efficiency is expressed as a function of the separation distance ρ by means of Eq. (2). This constraints divides the design space as shown in Figure 7.

The atmospheric drag force can be modeled in the usual way:

$$F_{\text{drag}} = \frac{1}{2}\, \varrho_{\text{atm}}\, C_D\, A\, v_r^2$$

where the atmospheric density ϱ_{atm} and the velocity relative to the atmosphere v_r depend on the orbit, and the cross-section area of the target can be estimated from the equivalent radius of the target, $A = \pi\, R_T^2$.

3.6. Maximum Thrust

Thrusters cannot operate at power levels $P > P_{\max}$. Since $F_2 > F_1$ during deorbiting operations, the former limitation imposes an upper boundary to the thrust provided by the secondary thruster, i.e. $F_2 \leqslant F_{\max}$. Using Eq. (1) the latter constraint may be reformulated as

$$\mathcal{C}^{(6)}(F_1, \rho) \equiv F_{\max} - F_1 \left(1 + \eta_B(\rho)\frac{m_S}{m_T}\right) \geqslant 0 \tag{24}$$

that partitions the design space as shown in Figure 8.

Note that the constraint imposed by the maximum thrust level depends on parameters of the plasma plume (most importantly the initial divergence angle φ), the size of the target body (by means of its equivalent radius R_T) and the

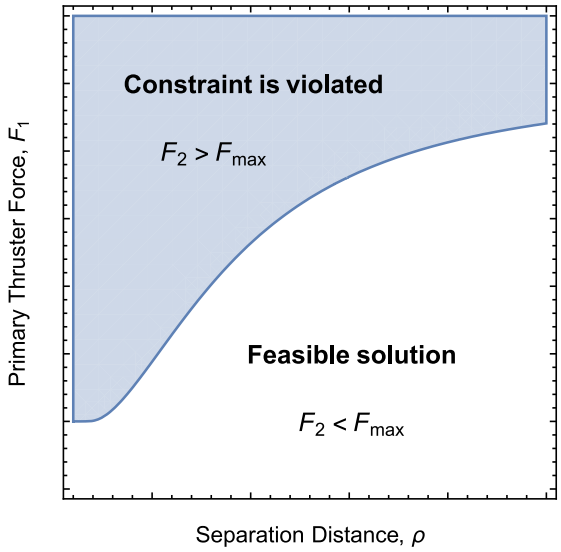

Figure 8: Region of the design space delimited by the constraint of maximum thrust.

mass ratio between the IBS satellite and the target object. Figure 9 shows how these parameters have a direct impact in the design space. In particular, the feasible design space will be larger when: 1) the divergence φ is increased; 2) the target size R_T is minimized; and 3) the more lightweight the IBS satellite is as compared to the target body. The latter point is of paramount importance in proximity operations, as it is directly related to the maneuverability of the IBS; the heavier the IBS, the larger the differential thrust between the primary and secondary thrusters will need to be in order to match the relative drift of the target with respect to the IBS and thus keep their separation constant. Also, note that the IBS-to-target mass ratio will change during the mission as the IBS consumes propellant and hence becomes more lightweight, which will naturally tend to enlarge the feasible region of the design space as the mission goes on.

3.7. Maneuverability and Control

In line with the previous discussion, the maneuverability of the IBS in its relative motion around the target is of the uttermost importance to ensure that

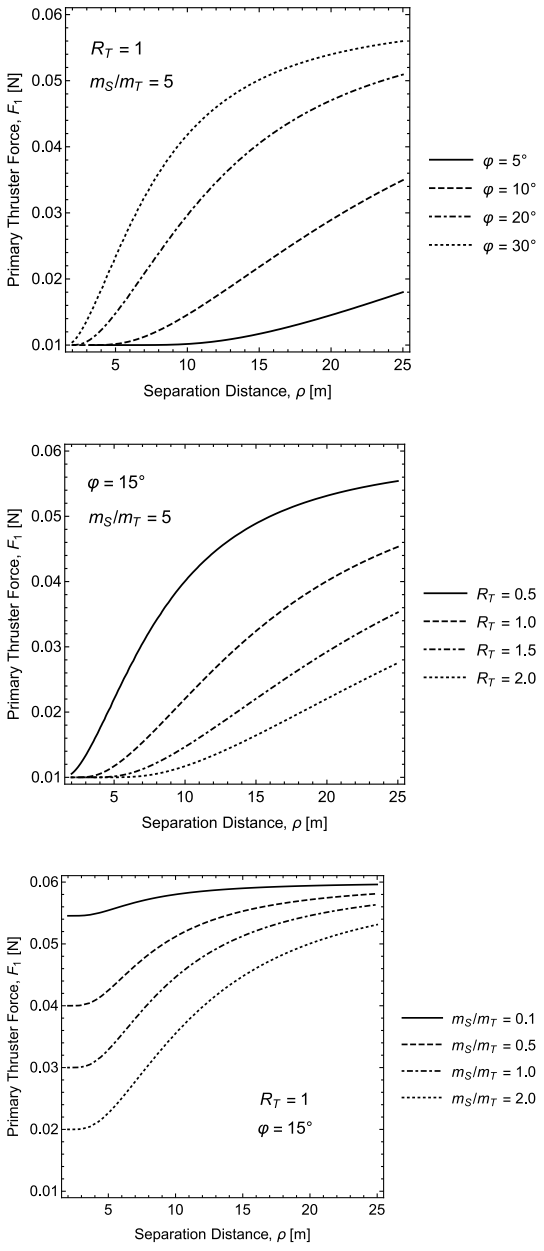

Figure 9: Dependence of the implicit function $F_2(F_1, \rho) = F_{\max}$ with the parameters φ, R_T and m_S/m_T, assuming a value $F_{\max} = 60$ mN.

the nominal separation distance ρ can be effectively controlled within operational limits. The control of the IBS-target relative position requires actuators capable of providing the necessary thrust to compensate any sudden perturbation and bring the IBS back into the nominal configuration. Alternatively, more sophisticated control strategies may allow the IBS to librate around the nominal relative position. Either way, the capability of providing a suitable control thrust is necessary. Interestingly, in order to control the along-track relative position, it might be an efficient strategy to rely on the throtability of the main thrusters. Under this assumption, it becomes necessary that none of the thrusters operate at maximum power, thus leaving a margin or extra thrust that can be employed for control purpose. In normal deorbiting operations $F_2 > F_1$, and hence it is the secondary thruster that needs to be limited, such that $F_2 < F_{\max}$. It seems reasonable that this control force budget, $F_{\max} - F_2$, be proportional to the actual acceleration transmitted to the target

$$F_{\max} - F_2 \geqslant \kappa\, \eta_B F_1\, \frac{m_S}{m_T}$$

where κ quantifies the margin of throtability that is saved for control purposes. By means of Eq. (1) this contraint can be expressed as

$$\mathcal{C}^{(7)}(F_1, \rho) \equiv F_{\max} - F_1 \left(1 + (1+\kappa)\, \eta_B(\rho)\, \frac{m_S}{m_T}\right) \geqslant 0 \tag{25}$$

By analogy with Ineq. (24), this constraint is equivalent to: 1) assuming an apparent momentum transfer efficiency $1+\kappa$ times larger than the actual value; or 2) assuming an apparent mass ratio $1+\kappa$ times larger than the actual value. The effect of this constraint is to shrink the feasible design space accordingly, as inferred from Figures 8 and 9.

3.8. Onboard Power Limitations

Though each of the main thrusters may in principle provide a maximum thrust $F_{\max}$, in practice, the limited power availability onboard the IBS satellite will likely prevent this situation. Thus, the combined power consumption of the

primary and secondary thrusters, P_1 and P_2 respectively, shall not exceed the total power available for the propulsion system, namely, $P_{\mathrm{PS,max}}$. Therefore, the operational regime of the thrusters shall comply with this limitation, that can be stated as $P_{\mathrm{PS}} \leqslant P_{\mathrm{PS,max}}$. Expressing the actual power supply for the propulsion system as a function of F_1 by virtue of Eq. (11), the power limitation constraint yields the following inequality:

$$\mathcal{C}^{(8)}(F_1, \rho) \equiv 2\,\alpha + \beta\,\eta_{\mathrm{PPU}}\,P_{\mathrm{PS,max}} - F_1\left(2 + \eta_B(\rho)\,\frac{m_S}{m_T}\right) \geqslant 0. \tag{26}$$

Comparing the latter equation with Ineq. (24) highlights that this constraint is formally (and qualitatively) similar to the maximum thrust constraint, and it will thus partition the design space in a similar fashion. However, the power limitation constraint will be more restraining than the maximum thrust constraint, and will thus shrink the feasible design space.

3.9. Backsputtering Contamination

As suggested in Subsection 2.5, the exposure of the IBS spacecraft to the flow of eroded material backsputtered from the target may contaminate sensitive surfaces of the IBS. This imposes a new type of limitation to the separation distance and thrust level at which the IBS can operate, and thus needs to be considered as an additional constraint to the design. This constraint can be stated as a threshold value to the cumulative contamination over the mission lifetime, or alternatively, as a maximum allowable deposition rate of contaminants on a prescribed reference surface, $\dot{h}_{\mathrm{max}}$. For this purpose, design guidelines are available where the contaminant layer thickness is correlated to the degradation of spacecraft equipment (e.g. solar arrays, optical sensors or thermal control surfaces) for various degrees of standardized molecular cleanliness levels [32].

The analytical approximation of the backsputtering deposition rate presented in Eqs. (15-16) proves valuable to this end, and allows to express the backsputtering contamination constraint as

$$\mathcal{C}^{(9)}(F_1, \rho) \equiv \dot{h}_{\mathrm{max}} - \dot{h}\,(F_1, \rho) \geqslant 0. \tag{27}$$

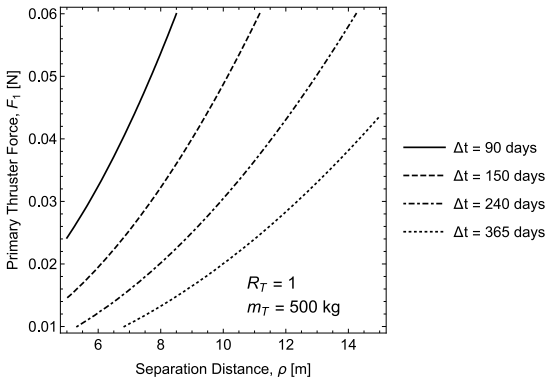

Figure 10: Constant deorbiting time contour lines for $r_0 = 7078$ km and $r_f = 6778$ km assuming a continuous thrust, even during eclipse.

This constraint partitions the design space following contour lines of constant deposition rate, as shown in Figure 5.

3.10. Mission Lifetime

The mission lifetime or deorbiting time might also play a significant role in the design of an IBS space mission. Due to operational considerations the mission lifetime, Δt, may need to be kept bound within a prescribed limit, $\Delta t_{\max}$, which would impose an additional design constraint. By virtue of Eq.(17), the maximum mission lifetime constraint can be expressed as

$$\mathcal{C}^{(10)}(F_1, \rho) \equiv \Delta t_{\max} - \Delta t\,(F_1, \rho) \geqslant 0. \tag{28}$$

This constraint partitions the design space following contour lines of constant deorbiting time, as shown in Figure 10.

3.11. Other Considerations

Apart from the design constraints considered so far, there are also other considerations that may have an impact in the technical design of an IBS mission, yet have been disregarded in this study. Such considerations may include: cost

constraints, launcher constraints, service policies, technology constraints, space debris mitigation policies, political and liability issues, etc. New restrictions on a technical or engineering ground could be, in most cases, incorporated to this analysis in a similar way; constraints of a political, legislatory or strategical nature, however, will likely require a different approach, and are therefore beyond the scope of this study.

4. Example Design Case

In this section we show an example of an IBS mission design case. Table 1 summarizes the design parameters and constraints, and Figures 11 and 12 display the corresponding design envelope and constraints. Note this is merely an example to illustrate the applicability of the design envelope or matching chart concept, and thus the values of Table 1 are chosen to be representative of a fictitious but credible mission. In the proposed example, the aim of the mission is to deorbit a 500 kg object from 700 km to 500 km altitude within 150 days, using two thrusters with thrust $F = 20\,\text{mN}$ to $60\,\text{mN}$ and a maximum power of 3.3 kW available for the exclusive use of the propulsion system.

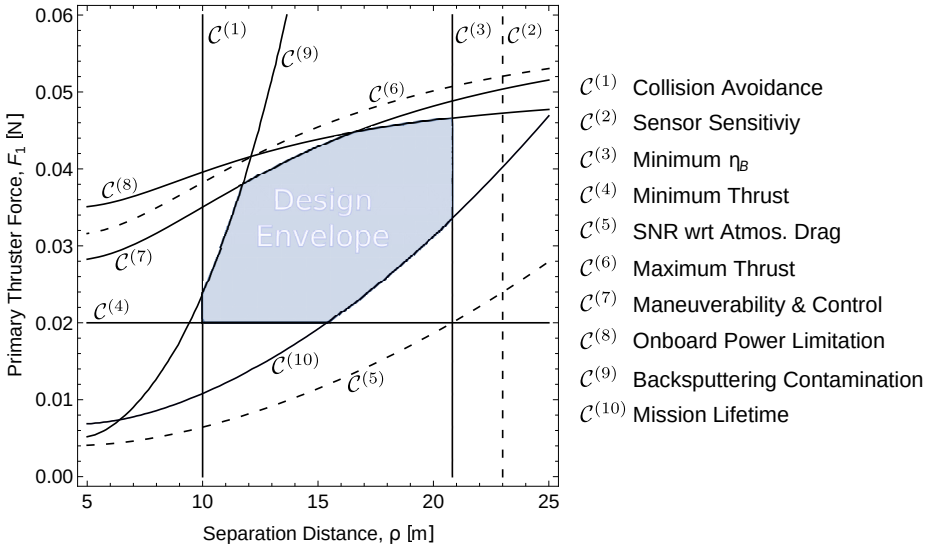

Figure 11: Design constraints of the example design case described in Table 1.

As observed from Fig. 11, the minimum separation distance would typically be delimited by either the backsputtering contamination or collision avoidance constraints, whereas the maximum separation distance would be restrained by either the mission lifetime, SNR with respect to atmospheric drag, minimum momentum transfer efficiency or the sensor sensitivity. Likewise, the minimum thrust level of the primary engine would be constrained by either the minimum thrust at which the thrusters can operate, the mission lifetime or the SNR with respect to atmospheric drag, whereas the maximum thrust level would be delimited by the backsputtering contamination, maneuverability & control issues, maximum thrust or onboard power limitations.

In order to select a design point within the envelope (i.e. a combination of nominal separation distance and thrust value), it is necessary to understand what the implications are and how the actual design varies as the design point moves across the domain of feasible solutions. For this aim, it is convenient to superimpose contour plots that provide additional information, or potentially, the values of an objective function that needs to be optimized in the design, e.g. the IBS mass, the onboard power, the mission duration or the cost. In this regard, the separation distance between the IBS spacecraft and the target object correlates with the momentum transfer efficiency by means of Eq. (2), such that a smaller separation distance yields a larger momentum transfer efficiency. This implies a more efficient propellant usage and a weight reduction (thus a cost reduction), but also a larger net force upon the target, and therefore a reduced deorbiting time (see Fig. 12), which ultimately also reverts into reductions of operational costs. Therefore, from this standpoint, it is reasonable to operate as close as possible to the target object.

Likewise, operating at a higher thrust level (i.e. higher value of F_1) will increase the net momentum transfered to the target body, and hence reduce the deorbiting time. However, this would also increase the backsputtering flux upon the IBS spacecraft, thus limiting the minimum separation distance (i.e. forcing the IBS to operate further away) and ultimately penalizing the transfered momentum. On the contrary, operating at a lower thrust value has benefi-

cial consequences, since not only the IBS could operate closer to the target, but also the propulsive requirements of the IBS spacecraft, and therefore its power requirements, would be less demanding (see Fig. 12). Additionally, since the spacecraft mass primarily scales with the power requirements by virtue of Eq. (12), a lower nominal thrust allows for a more lightweight IBS spacecraft, and ultimatly a lower cost. From this point of view, operating at a lower thrust level and hence reducing the power demand seems a desirable design criteria.

Under the aforementioned considerations, the preferred design point should ideally be close to the lower-left corner of the design envelope, since this would yield a balance between a lower thrust (lightweight spacecraft) and a higher momentum transfer efficiency (less propellant and shorter deorbiting time), whilst complying with the prescribed design and operational limitations. Interestingly, moving the design point towards the top-left corner would trade off a smaller momentum transfer efficiency and a higher thrust (ultimately larger IBS mass) in the benefit of a reduced deorbiting time. Consequently, the region of interest for practical design purposes lies on the leftmost edge of the design envelope.

At the light of these observations, an obvious consequence for the design of the particular example mission of Table 1 is that the maximum power $P_{\mathrm{PS,max}}$ is not a critical constraint. In fact, a lower value of $P_{\mathrm{PS,max}}$ (which would lower the onboard power limitation constraint curve in Fig. 11 would not handicap the mission; on the contrary, it proves the mission could be accomplished with a lower power level, and thus smaller solar arrays, reduced battery capacity, and ultimately a smaller mass. Therefore, the design methodology presented in this article not only allows to obtain a preliminary design of an IBS mission, but also provides a valuable insight in the key design constraints and guidance on how the design can be modified to meet specific requirements and comply with specific considerations.

5. Further Discussion

It is important to highlight the fact that even though the design envelope or matching chart is constructed from the most limiting values of the design constraints, some of them actually have a dynamic nature in the sense that the actual or instantaneous limitations that they impose may change or evolve over time. For instance, the IBS mass will decrease as propellant is consumed (although mass variations are typically small due to high I_{sp} thrusters), atmospheric density will increase as the orbital radius decreases, the thruster performance and available power will undergo a degradation over the mission lifetime, etc., thus affecting the constraints that depend on the aforementioned parameters. Therefore, the boundaries delimited by the instantaneous design and operational constraints are not fixed throughout the mission; however, for design purposes, the most limiting cases must be assumed (by fixing parameters to their most stringent values), which often correspond to the initial or final configuration of the mission (e.g. initial mass of the shepherd, atmospheric density at the lowest altitude, power availability and thrust parameters at the end of the mission lifetime, etc.). As a result, the selection of the design point within the matching chart is based on the most stringent realizations of the aforementioned contraints, such that their time-dependence is removed. Consequently, the design point represents the nominal values of the separation distance and thrust level, i.e. the nominal operation point of the IBS system. These values represent the stationary working point of the system, and are meant to remain constant for the duration of the mission.

Likewise, the same set of variables (namely, separation distance and primary thrust) can also be used to describe the instantaneous working point of the IBS system (i.e. the actual operation point), and might therefore represent transient values that can depart from the intended nominal or design values. When that occurs, the design envelope might instead play the role of a *flight envelope* (by analogy with the aircraft design nomenclature), which identifies the set of possible states of the system (i.e. feasible working points) regardless of whether these

are transient or stationary working points. This offers a dual interpretation of the matching chart, i.e.: 1) a diagram intended for design purposes, where the feasible design region is bounded by fixed and immutable constraints, and the nominal operation point can be set; and 2) a diagram intended to parameterize the actual operation point, where some of the boundaries of the feasible design region may cease to apply or can be trespassed without incurring in any infeasibility. This paves the way to classifying the constraints introduced in Section 3 as either *hard* or *soft* constraints.

Hard constraints are those that under no circumstance can be overstepped without violating physical limitations or defying safety considerations. For example, the collision avoidance constraint is a hard constraint that cannot be violated without jeopardizing the mission; likewise, performing below the minimum thrust level of a thruster is physically unachievable, and therefore the minimum thrust constraint is also a hard limit.

On the other hand, we refer to soft constraints when these can be temporarily exceeded without irreversible adverse implications upon the system. For instance, operating at a lower momentum transfer efficiency than the prestablished threshold is undesirable from an efficiency point of view, but other than that, the IBS system can perform normally without meeting that restriction. Another example of a soft constraint is the backsputtering contamination constraint; this limitation is based on the accumulated contamination level assuming a constant backsputtering flow, but an IBS could temporarily operate beyond such threshold (i.e. receiving a bigger dose of contamination), as long as the backsputtering overexposure is followed by a transient stage of underexposure, for compensation.

6. Conclusions

This article presents a preliminary design methodology for an ion-beam shepherd mision for active space debris removal. This method uses a matching chart approach, which allows to account for different design and operational con-

straints. Hence, the design space is partitioned into: 1) a feasible solution subspace, where all constraints are met; and 2) forbidden regions, where constraints are violated.

The preliminary design of an ion-beam shepherd mission can be synthesized to a point in a bi-parametric design space; thus, ultimately the mission design stems from two key parameters only, namely the separation distance with respect to the target object to be deorbited, and the thrust level. Interestingly, the different constraints upon the design can be analytically expressed and graphically represented as curves in the design space, thus delimiting the region of feasible solutions that comply with all applicable constraints and requirements. Specifically to an ion-beam shepherd mission, the constraints considered in this article include limitations due to: collision avoidance, sensor sensitivity, minimum momentum transfer, minimum thrust, maximum thrust, signal-to-noise ratio with respect to atmospheric drag, maneuverability and control, onboard power availability, backsputtering contamination, and mission lifetime (deorbit time).

The concept of the design envelope presented in this article proves a useful construction for the preliminary design of an ion-beam shepherd mission, offers a valid methodology for this purpose, and provides a valuable insight on the key design drivers.

Acknowledgments

This research was supported and funded by the research grant ESP2017-87271-P (MINECO/AEI/FEDER,UE).

Appendix A. Analytical Backsputtering Contamination Model

For an IBS mission, assuming a spherical target object of radius R_T located on the plasma beam centerline at a distance ρ from the origin of a conical plasma plume of semi-angle φ, the differential sputtering yield emanated from a given

point of the target surface can be modeled following Sigmund's theory [33] as

$$y(\vartheta) = \frac{Y\,\cos(\vartheta)}{\pi}$$

where the sputtering yield Y can be evaluated as a function of the energy of the incoming ions, the incidence angle and the materials of the ion and the target surface, and ϑ indicates the direction (with respect to the surface normal) of the sputtering recoil flux. Due to the axisymmetry of this configuration (see Figure A.13), the total backsputting flow emanated from the target sphere and measure at the vertex of the conical plasma beam is given by the integral

$$\Phi = 4\pi \int_0^{\theta^*} y(\vartheta)\, n(\theta)\, \frac{R_T^2}{\varrho^2}\, \sin(\theta)\, \mathrm{d}\theta$$

where the angle θ defines the position of every area element of the target, θ^* is the upper bound for the integral, ϱ is the distance from the plasma source to the area element, and $n(\theta)$ is the plasma density. Every area element of the sphere has a radial position component $\hat{R}$ measured from the beam centerline, and an axial position component d, as illustrated in Fig. A.13.

From geometrical considerations, the following relations hold:

$$\hat{R} = \varrho\, \sin\psi, \qquad d = \varrho\, \cos\psi$$
$$\hat{R} = R_T\, \sin\theta, \qquad d = \rho - R_T\, \cos\theta$$

additionally,

$$\varrho = \rho\, \Lambda(\theta), \qquad \Lambda(\theta) = \sqrt{1 - 2\epsilon\, \cos\theta + \epsilon^2}$$

where the parameter $\epsilon = R_T/\rho$ is defined for brevity. Therefore:

$$\sin\psi = \frac{\epsilon\, \sin\theta}{\Lambda(\theta)}, \qquad \cos\psi = \frac{1 - \epsilon\, \cos\theta}{\Lambda(\theta)}$$

The particular geometry of Fig. A.13 yields the constraint $\vartheta = \psi + \theta$, and thus

$$\cos\vartheta = \frac{\cos\theta - \epsilon}{\Lambda(\theta)}$$

Under the simplifying assumptions of a conical plasma plume, the plasma density can be modeled as [24, 14]

$$n(d,\hat{R}) = \frac{3\,n_0}{(d\,\tan\varphi)^2}\exp\left(\frac{-3\hat{R}^2}{(d\,\tan\varphi)^2}\right)$$

where n_0 is the density at the plasma source. After a change of variables, the density can be expressed as a function of θ and ϵ, as follows:

$$n(\theta;\epsilon) = \frac{3\,n_0\,\epsilon}{\left[R_T(1-\epsilon\,\cos\theta)\tan\varphi\right]^2}\exp\left[-3\left(\frac{\epsilon\,\sin\theta}{(1-\epsilon\,\cos\theta)\,\tan\varphi}\right)^2\right]$$

Thus, the backsputtering flow can be written entirely as a funcion of θ, which takes the following form:

$$\Phi(\epsilon) = \frac{12\,n_0\,Y}{\tan^2\varphi}\frac{\epsilon^4}{R_T^2}\int_0^{\theta^*}\frac{\cos\theta-\epsilon}{\Lambda^3(\theta)}\frac{\sin\theta}{(1-\epsilon\,\cos\theta)^2}\exp\left[-3\left(\frac{\epsilon\,\sin\theta}{(1-\epsilon\,\cos\theta)\,\tan\varphi}\right)^2\right]\mathrm{d}\theta$$

This expression can be written in a more convenient form after the change of variables $u=\cos\theta$, which yields

$$\Phi(\epsilon) = \frac{12\,n_0\,Y}{\tan^2\varphi}\frac{\epsilon^4}{R_T^2}\int_0^{u^*}\frac{\epsilon-u}{\Lambda^3(\theta)\,(1-\epsilon\,u)^2}\exp\left[-3\left(\frac{\epsilon\sqrt{1-u^2}}{(1-\epsilon\,u)\,\tan\varphi}\right)^2\right]\mathrm{d}u$$

where the upper bound of the integral is

$$u^* = \cos(\theta^*) = \frac{R_T}{\rho} = \epsilon$$

as can be obtained from simple geometrical considerations for the case of a grazing ion tangent to the sphere.

The parameter ϵ is small for cases of interest, enabling to expand the former integrand in Taylor series, leading to

$$\Phi(\rho) = C\,\frac{R_T^2\left[(6\rho^2-R_T^2)\tan^2\varphi-3R_T^2\right]}{\rho^6\,\tan^3\varphi}$$

where C is a constant to be determined. Note that the integration constant must be zero, since the backsputtering flow must vanish when $\rho\to\infty$.

The plasma density and the sputtering yield both depend on the thrust level provided by the ion engine; thus, the constant C must be a function of the

primary thrust F_1. Upon observation of the numerical simulation results, the following fitting function proves to conveniently match the results:

$$C(F_1) = \phi \tanh^{\sigma}(F_1)$$

where ϕ and σ are fitting parameters to be determined upon numerical or experimental results, thus resulting in the analytical backsputtering contamination model of Eq. (15).

References

[1] J.-C. Liou, N. L. Johnson, Risks in space from orbiting debris, Science 311 (5759) (2006) 340–341. doi:10.1126/science.1121337.

[2] J.-C. Liou, N. L. Johnson, Instability of the present LEO satellite populations, Advances in Space Research 41 (7) (2008) 1046–1053. doi:10.1016/j.asr.2007.04.081.

[3] IADC space debris mitigation guidelines, Tech. rep., Inter-Agency Space Debris Co-ordination Committee (2007).
URL http://www.iadc-online.org

[4] Space debris mitigation guidelines of the committee on the peaceful uses of outer space, Tech. rep., United Nations, Office for Outer Space Affairs, Vienna (2010).
URL http://www.unoosa.org/pdf/publications/st_space_49E.pdf

[5] J.-C. Liou, N. L. Johnson, A sensitivity study of the effectiveness of active debris removal in leo, Acta Astronautica 64 (23) (2009) 236–243. doi:10.1016/j.actaastro.2008.07.009.

[6] J.-C. Liou, N. L. Johnson, N. M. Hill, Controlling the growth of future LEO debris populations with active debris removal, Acta Astronautica 66 (5-6) (2010) 648–653. doi:10.1016/j.actaastro.2009.08.005.

[7] J.-C. Liou, An active debris removal parametric study for LEO environment remediation, Advances in Space Research 47 (11) (2011) 1865–1876. doi:10.1016/j.asr.2011.02.003.

[8] A. E. White, H. G. Lewis, The many futures of active debris removal, Acta Astronautica 95 (2014) 189–197. doi:10.1016/j.actaastro.2013.11.009.

[9] A. E. White, H. G. Lewis, An adaptive strategy for active debris removal, Advances in Space Research 53 (8) (2014) 1195–1206. doi:10.1016/j.asr.2014.01.021.

[10] M. Shan, J. Guo, E. Gill, Review and comparison of active space debris capturing and removal methods, Progress in Aerospace Sciences 80 (2016) 18–32. doi:10.1016/j.paerosci.2015.11.001.

[11] C. Bombardelli, J. Peláez, Ion beam shepherd for contactless space debris removal, Journal of Guidance, Control and Dynamics 34 (3) (2011) 916–920. doi:10.2514/1.51832.

[12] C. Bombardelli, J. Peláez, Ion beam shepherd for asteroid deflection, Journal of Guidance, Control and Dynamics 34 (4) (2011) 1270–1272. doi:10.2514/1.51640.

[13] C. Bombardelli, H. Urrutxua, M. Merino, J. Pelez, E. Ahedo, The ion beam shepherd: A new concept for asteroid deflection, Acta Astronautica 90 (1) (2013) 98 – 102, selected Papers from the 2011 IAA Planetary Defense Conference. doi:10.1016/j.actaastro.2012.10.019.
URL http://www.sciencedirect.com/science/article/pii/S0094576512003979

[14] C. Bombardelli, Ion beam technology for space debris mitigation, in: Space Debris Reentry and Mitigation, no. 16 in STO-AVT-262, von Karman Institude for Fluid Dynamics, Belgium, 2016, pp. 1–20.

URL http://sdg.aero.upm.es/PUBLICATIONS/PDF/2017/Bombardelli_VKI_LS_IBS.pdf

[15] LEOSWEEP, FP7 Project Website (2013).
URL https://leosweep.upm.es

[16] W. J. Larson, J. R. Wertz, Space Mission Analysis and Design, Microcosm Press and Kluwer Academic Publishers, 1999.

[17] T. Mosher, Conceptual spacecraft design using a genetic algorithm trade selection, Journal of Aircraft 363636 (1) (1999) 200–208. doi:10.2514/2.2426.

[18] J. Gross, S. Rudolph, Modeling graph-based satellite design languages, Aerospace Science and Technology 49 (2016) 63 – 72. doi:10.1016/j.ast.2015.11.026.
URL http://www.sciencedirect.com/science/article/pii/S1270963815003703

[19] J. Gross, S. Rudolph, Rule-based spacecraft design space exploration and sensitivity analysis, Aerospace Science and Technology 59 (2016) 162 – 171. doi:10.1016/j.ast.2016.10.007.
URL http://www.sciencedirect.com/science/article/pii/S1270963816308471

[20] F. Cichocki, M. Merino, E. Ahedo, M. Smirnova, A. Mingo, M. Dobkevicius, Electric propulsion subsystem optimization for "ion beam shepherd" missions, Journal of Propulsion and Power 33 (2) (2017) 370–378. doi:10.2514/1.B36105.

[21] E. Torenbeek, Synthesis of Subsonic Airplane Design, Delft University Press, Kluwer Academic Publishers, 1976.

[22] M. Merino, F. Cichocki, E. Ahedo, A collisionless plasma thruster plume expansion model, Plasma Sources Science and Technology 24 (3) (2015) 1–12. doi:10.1088/0963-0252/24/3/035006.

[23] C. Bombardelli, M. Merino, E. Ahedo, J. Peláez, H. Urrutxua, J. Herrera-Montojo, A. Iturri-Torrea, J. Olympio, D. Petkow, L. Summerer, Ion beam shepherd for contactless debris removal, Tech. rep., European Space Agency (2011).
URL http://www.esa.int/gsp/ACT/doc/ARI/ARI%20Study%20Report/ACT-RPT-MAD-ARI-10-6411c-1107-FR-Ariadna-Ion_Beam_Shepherd_Madrid_4000101447.pdf

[24] C. Bombardelli, H. Urrutxua, M. Merino, E. Ahedo, J. Peláez, Relative dynamics and control of an ion beam shepherd satellite, in: Advances in the Astronautical Sciences, Vol. 143, Univelt, 2012, pp. 2145–2157, paper AAS 12-246.

[25] A. Alpatov, F. Cichocki, A. Fokov, S. Khoroshylov, M. Merino, A. Zakrzhevskii, Determination of the force transmitted by an ion thruster plasma plume to an orbital object, Acta Astronautica 119 (2016) 241–251. doi:10.1016/j.actaastro.2015.11.020.

[26] F. Cichocki, M. Merino, E. Ahedo, Spacecraft-plasma-debris interaction in an ion beam shepherd mission, Acta Astronautica 146 (2018) 216 – 227. doi:https://doi.org/10.1016/j.actaastro.2018.02.030.
URL http://www.sciencedirect.com/science/article/pii/S0094576517316739

[27] M. G. Marcucci, J. E. Polk, NSTAR xenon ion thruster on deep space 1: Ground and flight tests, Review of Scientific Instruments 71 (3) (2000) 1389–1400. doi:10.1063/1.1150468.

[28] H. Urrutxua, High fidelity models for near-earth object dynamics, Ph.D. thesis, Universidad Politécnica de Madrid (2015).
URL http://oa.upm.es/35503/1/HODEI_URRUTXUA_CEREIJO.pdf

[29] H. Urrutxua, C. Bombardelli, IBIS: Exploring a safe exploitation of space (2015).

URL http://www.upm.es/observatorio/vi/index.jsp?pageac=innovacion/articulo.jsp&id_tipo_articulo=3&id_articulo=296

[30] O. B. Duchemin, J. R. Brophy, C. E. Garner, P. K. Ray, V. Shutthanandan, M. A. Mantenieks, A review of low energy sputtering theory and experiments, Tech. Rep. 97-1081, NASA JPL (1997).
URL http://hdl.handle.net/2014/22572

[31] Z. L. Zhang, L. Zhang, Anisotropic angular distributions of sputtered atoms, Radiation Effects and Defects in Solids 159. doi:10.1080/10420150410001724495.

[32] A. C. Tribble, B. Boyadjian, J. Davis, J. Haffner, E. McCullough, Contamination control engineering design guidelines for the aerospace community, Tech. Rep. NASA Contractor Report 4740, Rockwell International Corporation, Downey, CA (May 1996).

[33] P. Sigmund, Theory of sputtering. i. sputtering yield of amorphous and polycrystalline targets, Phys. Rev. 184 (1969) 383–416. doi:10.1103/PhysRev.184.383.
URL https://link.aps.org/doi/10.1103/PhysRev.184.383

Table 1: Parameters for the example design case. Note that m_S and m_{prop} are not parameters, but derived quantities computed from Eq. (12) and Eq. (14), respectively; they are included here for the sake of completeness and reproducibility.

	Parameters	Values	Units
Target body	m_T	500	kg
	R_T	1.0	m
Shepherd Satellite	m_S	456.7	kg
	m_{prop}	44.2	kg
	$m_{\text{prop,RCS}}$	15	kg
	m_0	150	kg
	α_P	75	$\text{kg}\,\text{kW}^{-1}$
	R_S	1.0	m
	η_{PPU}	0.9	-
	P_{other}	500	W
	$P_{\text{PS,max}}$	2800	W
	$P_{\text{Total,max}}$	3300	W
Thruster and plume	F_{max}	60	mN
	F_{min}	20	mN
	P_{max}	1500	W
	P_{min}	450	W
	$\dot{m}_{\text{max}}$	2.0	$\text{mg}\,\text{s}^{-1}$
	$\dot{m}_{\text{min}}$	0.8	$\text{mg}\,\text{s}^{-1}$
	γ'	0	$\text{mg}\,\text{s}^{-1}\,\text{W}^{-2}$
	φ	10	deg
Deorbiting	r_0	7078	km
	r_f	6878	km
	χ	0.378	-
	ϱ_{atm}	$2 \cdot 10^{-12}$	$\text{kg}\,\text{m}^{-3}$
	C_D	2.2	-
Backsputtering	σ	1.25	-
	ϕ	1/17000	$\text{kg}\,\text{m}^{-2}\,\text{s}^{-1}$
	ϱ_T	2700	$\text{kg}\,\text{m}^{-3}$
Constraints	ρ_{col}	10	m
	ρ_{sen}	23	m
	$\eta_{B,\text{min}}$ 43	0.2	-
	SNR	10	-
	κ	0.25	-
	$\dot{h}_{\text{max}}$	50	$\text{nm}\,\text{day}^{-1}$
	Δt_{max}	150	days

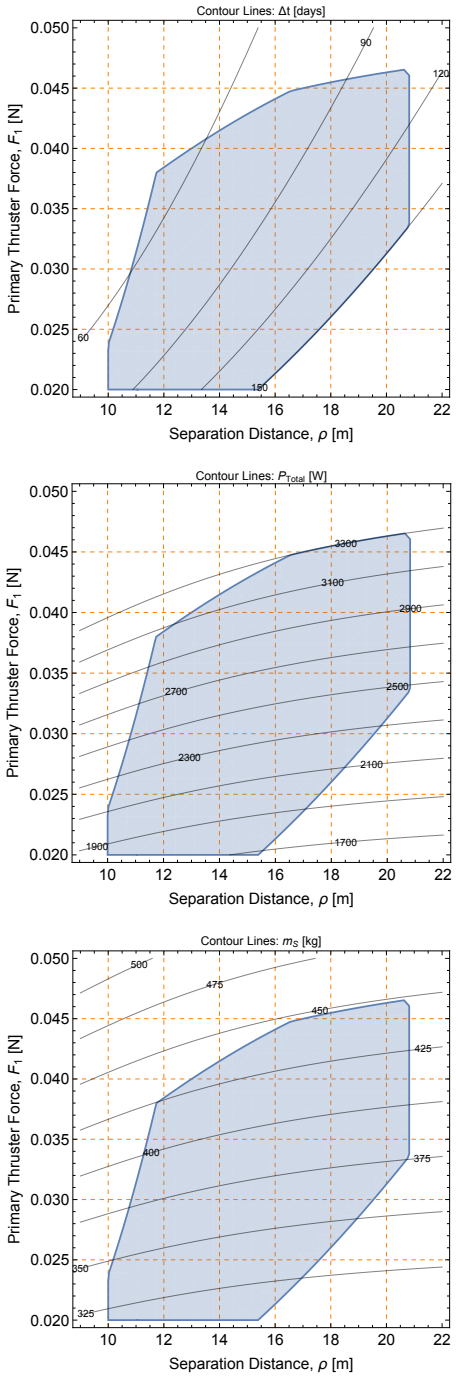

Figure 12: Design envelope of the example design case described in Table 1, including contour lines for constant values of Δt, P_{Total} and m_S, respectively.

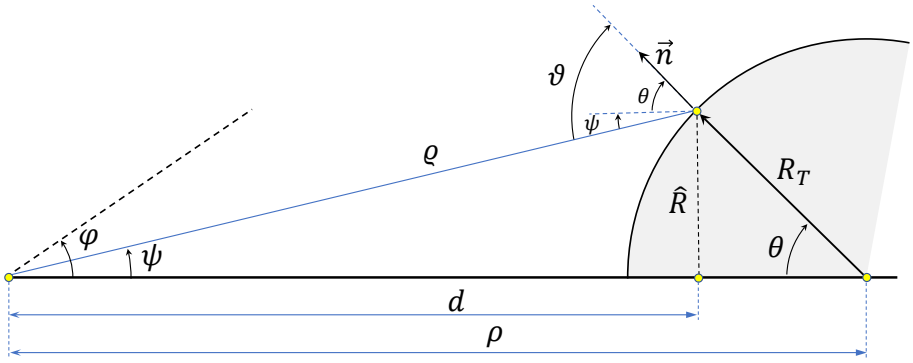

Figure A.13: Geometrical configuration of the case under study.